FFI RAPPORT

NUMERICAL SIMULATIONS OF FLOW-INDUCED VIBRATIONS ON ORION P-3C

REIF Bjørn A P, WASBERG Carl Erik

FFI/RAPPORT-2003/01331

FFIBM/820/170

Approved
Kjeller 2. April 2003

Bjarne Haugstad
Director of Research

NUMERICAL SIMULATIONS OF FLOW-INDUCED VIBRATIONS ON ORION P-3C

REIF Bjørn A P, WASBERG Carl Erik

FFI/RAPPORT-2003/01331

FORSVARETS FORSKNINGSINSTITUTT
Norwegian Defence Research Establishment
P O Box 25, NO-2027 Kjeller, Norway

FORSVARETS FORSKNINGSINSTITUTT (FFI)
Norwegian Defence Research Establishment

P O BOX 25
N0-2027 KJELLER, NORWAY

UNCLASSIFIED

SECURITY CLASSIFICATION OF THIS PAGE
(when data entered)

REPORT DOCUMENTATION PAGE

1) PUBL/REPORT NUMBER FFI/RAPPORT-2003/01331	**2) SECURITY CLASSIFICATION** UNCLASSIFIED	**3) NUMBER OF PAGES** 27
1a) PROJECT REFERENCE FFIBM/820/170	**2a) DECLASSIFICATION/DOWNGRADING SCHEDULE** -	

4) TITLE

NUMERICAL SIMULATIONS OF FLOW-INDUCED VIBRATIONS ON ORION P-3C

5) NAMES OF AUTHOR(S) IN FULL (surname first)

REIF Bjørn A P, WASBERG Carl Erik

6) DISTRIBUTION STATEMENT

Approved for public release. Distribution unlimited. (Offentlig tilgjengelig)

7) INDEXING TERMS

IN ENGLISH:	**IN NORWEGIAN:**
a) Flow-induced vibrations	a) Strømningsgenererte vibrasjoner
b) Computational fluid dynamics	b) Numerisk strømningsdynamikk
c) Turbulent wakes	c) Turbulente kjølvann
d) Vortex shedding	d) Virvelavløsning
e) Bluff-body flows	e) Strømning rundt butte legemer

THESAURUS REFERENCE:

8) ABSTRACT

The radome mounted on the Orion P-3C has a significant adverse impact on the performance of the aircraft. Measurements have revealed low-frequency vibrations so severe that operational restrictions have been imposed. This report gives a preliminary assessment of the fluid dynamical implications of the radome at different freestream velocities, based on computational fluid dynamics (CFD). The low-frequency vibrations are captured by the numerical simulations, and the results are in good agreement with existing literature with respect to the dominant flow field features. CFD is therefore believed to be a viable tool for improved design of the radome with the objective to reduce the amplitude of the unsteady fluid forcing

9) DATE 2. April 2003	**AUTHORIZED BY** This page only Bjarne Haugstad	**POSITION** Director of Research

ISBN 82-464-0702-3

UNCLASSIFIED

SECURITY CLASSIFICATION OF THIS PAGE
(when data entered)

CONTENTS

Page

1 INTRODUCTION 7

2 SOME FLUID DYNAMICAL ASPECTS 7
2.1 Infinite cylinders in cross-flow 8
2.2 Small aspect ratio effects 10

3 COMPUTATIONAL APPROACH 11
3.1 Two-dimensional simulations 12
3.2 Three-dimensional simulations 15

4 RESULTS 18
4.1 Flow field 18
4.2 Forces 21
4.2.1 Available structural measurements 21
4.2.2 Numerical results 21

5 CONCLUSIONS 25
References 26
Distribution list 27

NUMERICAL SIMULATIONS OF FLOW-INDUCED VIBRATIONS ON ORION P-3C

1 INTRODUCTION

Wall-mounted sensors and other devices that extend across external boundary layers into the freestream are present in many aero- and hydrodynamical applications. Although the size of these devices are usually small compared with the overall size of the vehicle, they can have significant impact on the performance, and in some cases even impose highly undesirable operational restrictions. One such example is the radome mounted on the Orion P-3Cs operated by the Royal Norwegian Air Force, see figure 2.1. Recent measurements [7, 8] have revealed significant structural vibrations due to this device. These low-frequency vibrations are in fact so severe that operational restrictions have been imposed on the aircraft.

This report gives a preliminary assessment of the fluid dynamical implications of the radome at different freestream velocities. The study is based on a computational fluid dynamics (CFD) approach which constitutes a feasible alternative to more expensive wind-tunnel or full-scale tests in order to assess aerodynamical implications of new configurations. The objective of this preliminary study is to compute the time-dependent force that arises due to the massive flow separation downstream of the radome. If CFD is found to be a useful tool to describe the unsteady phenomena observed during flight, it can also be used to assist the development of an improved design.

2 SOME FLUID DYNAMICAL ASPECTS

The terminology flow-induced vibrations alludes to the coupling between the forces exerted by the surrounding fluid motion on the mechanical structure, and to the dynamical response of the structure itself. This is in general a two-way coupling. However, we will neglect any deformation of the structure in this study and only consider the aerodynamical forces (pressure and viscous) that act on the radome.

Many hundreds of investigations of circular cylinders with large aspect ratios ($H/D \gg 1$, see figure 2.3) in cross flow have been reported over the years, see e.g. [2]. At large aspect ratios, the flow field remains virtually two-dimensional since end-wall effects can be neglected. There are however some other complicating features relevant for the present case that needs to be considered.

It is instructive to make a qualitative description of the complex flow field in the vicinity of the radome with reference to the well-documented effects related to large aspect ratio cylinders in a cross flow. Some of these classical results are therefore briefly summarized in the next section. Another, and an even more important, motivation of this is that there exist no reference data that enables us to perform quantitative validations of our computations. It

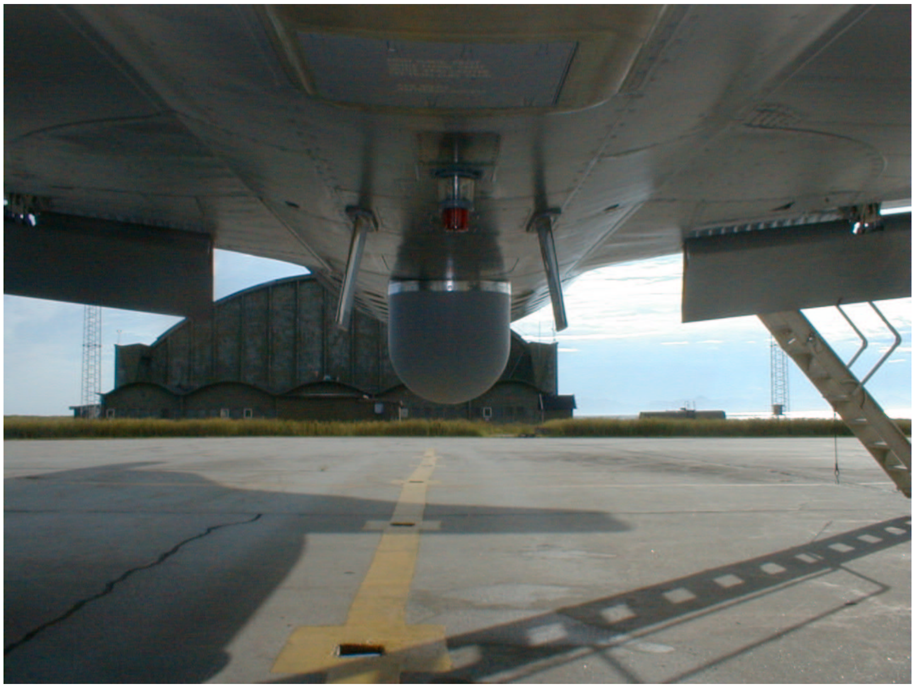

Figure 2.1: A backwards view of the radome under the airplane. Photo by Øistein Lundberg, FFI.

is therefore of utmost importance to establish confidence in our results based on qualitative comparisons with other relevant studies, including the classical infinite cylinder case. A rather comprehensive literature survey has therefore been conducted.

2.1 Infinite cylinders in cross-flow

Huerre and Monkewitz [6] described the absolute and convective instabilities in the near wake region of infinitely long cylinders as the primary mechanisms for the shedding behaviour. Controlling bluff-body flows in general could thus be achieved by affecting the flow field in this region. There exist experimental evidence that the two-dimensionality of the flow field remains a valid assumption as long as $H/D > 5$, in which case the classical results for infinitely long cylinders hold true [1].

Another important effect is the interaction between the two boundary layers with opposite sign of the vorticity ($\nabla \times \vec{U}$), that form on each side of the cylinder and the positions of the flow separation. The classical Karman vortex street that forms downstream of the cylinder is strongly affected by this dynamic interaction.

The dominating frequency of the shedding motion is usually expressed in term of a dimensionless parameter referred to as the Strohaul number which is defined as

$$\mathrm{St} = \frac{fD}{U_\infty}, \tag{2.1}$$

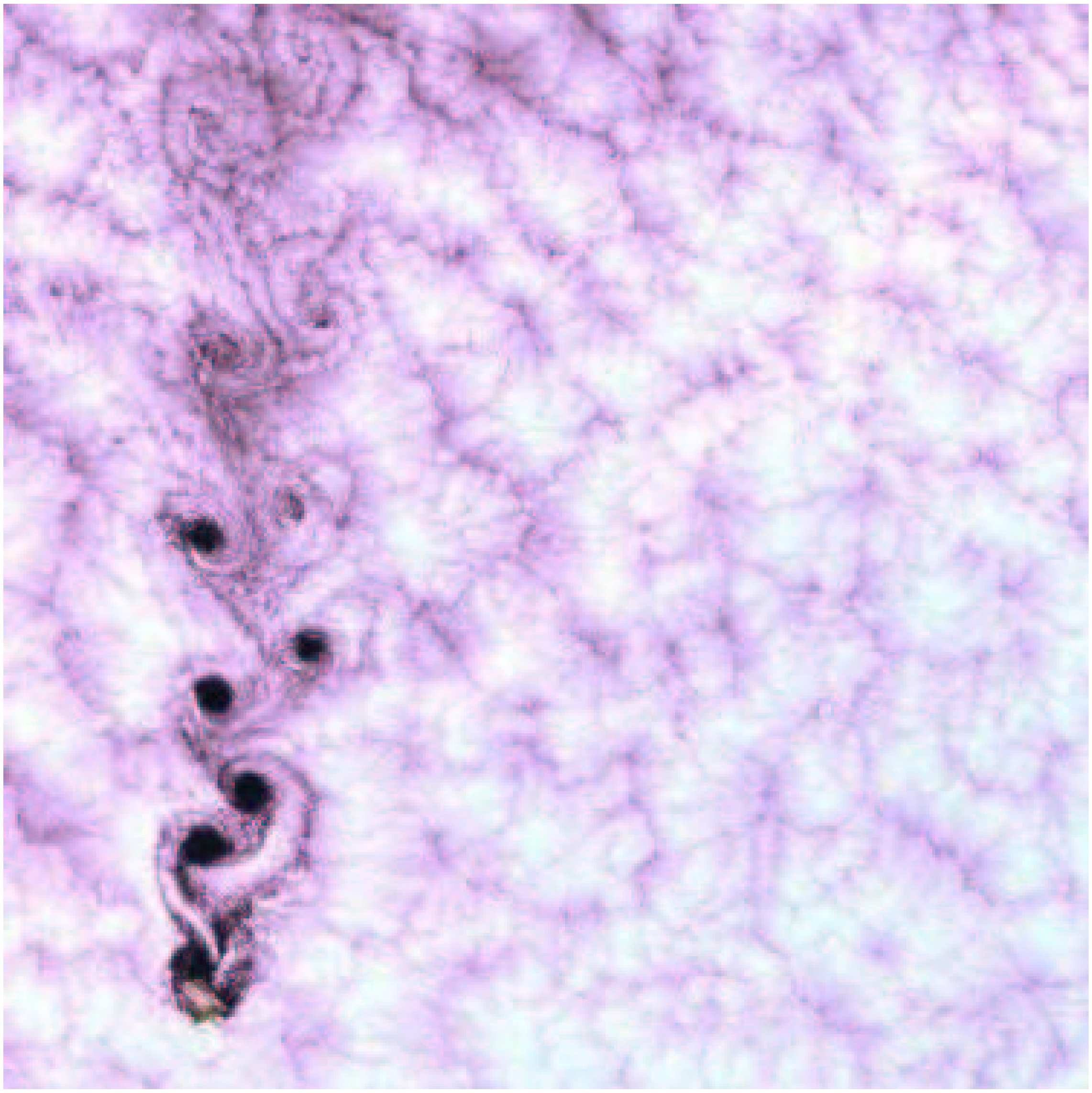

Figure 2.2: A rare meteorological phenomenon caught by LANDSAT 7 on 9/15/1999, taken from `www.efluids.com`*. In the lower left corner of the picture is Alejandro Selkirk Island, a squarish island that rises almost vertically 1 mile above the southern Pacific. A boundary layer that sandwiches a saturated, unstable layer of clouds between two more stable layers is broken by the island, causing a formation of vortices known as a Karman Vortex Street.*

where f is the dominating shedding frequency, D is the cylinder diameter and U_∞ is the freestream velocity, see figure 2.3. St has been found to vary in the range $0.1 < \mathrm{St} < 0.5$, depending on the Reynolds number

$$\mathrm{Re} = \frac{U_\infty D}{\nu}, \tag{2.2}$$

where ν is the kinematic viscosity. This non-dimensional parameter describes the ratio between inertial and viscous forces acting on a fluid element.

At $\mathrm{Re} < 10^5$ the boundary layers on the cylinder are laminar and thus also nearly two-dimensional. In the range $2 \times 10^5 < \mathrm{Re} < 3.5 \times 10^5$ the boundary layers become transitional and undergo a laminar-to-turbulent transition. In transitional boundary-layers, patches of laminar and turbulent motions co-exist. Due to the enhanced mixing of momentum, turbulent boundary layers do in general exhibit flow separation significantly further downstream than laminar boundary layers; the flow separation line on the cylinder surface has therefore a tendency to become wave-like in a transitional boundary layer rather than straight as observed for laminar, or fully turbulent, boundary layers. This lack of coherence along the cylinder axis is believed to suppress the classical shedding behaviour. In fact, it has been observed that the near-wake region becomes narrower and disorganized and the characteristic shedding motion is virtually annihilated in this range of Re, see e.g. [2].

At $\mathrm{Re} > 3.5 \times 10^5$ the vortex street is re-established and the shedding motion re-appear. At such high Re, the boundary layers have undergone a change of character from a transitional to a fully developed state. The axial coherence is thus increased which constitutes a possible explanation for the re-appearance of the shedding. This was first discovered by Roshko [9]. However, there are still a number of fundamental aspects of high Re bluff body flows that remain unanswered. These are all related to the physics of turbulence.

It should finally be mentioned that detailed laboratory measurements at $\mathrm{Re} > 10^6$ are difficult to conduct. The difficulty lies in the fact that the range of turbulent scales at high Re are so large that they are very difficult to measure; the scales are simply too small to be captured by present measurements technology [1]. The remedy to this problem would be to attain a high Re by a large diameter D and small kinematic viscosity ν, rather than by increasing the velocity U_∞. Figure 2.2 shows a rare meteorological phenomenon that confirms the re-establishment of the Karman vortex street at extreme Re.

2.2 Small aspect ratio effects

A schematic of the present case is shown in figure 2.3. It is rather different from the idealized infinite cylinder case: Firstly, the small aspect ratio $H/D \approx 1$, and secondly that the incoming boundary layer thickness $\delta \sim O(H)$. The small aspect ratio implies a

---

[1] The largest turbulent scales are in the order of the diameter D, whereas the smallest spatial scales are $d \sim D/\mathrm{Re}^{3/4}$ m. With $D = 0.65$ m and $\mathrm{Re} = 10^6$, $d \sim 2 \times 10^{-5}$ m!

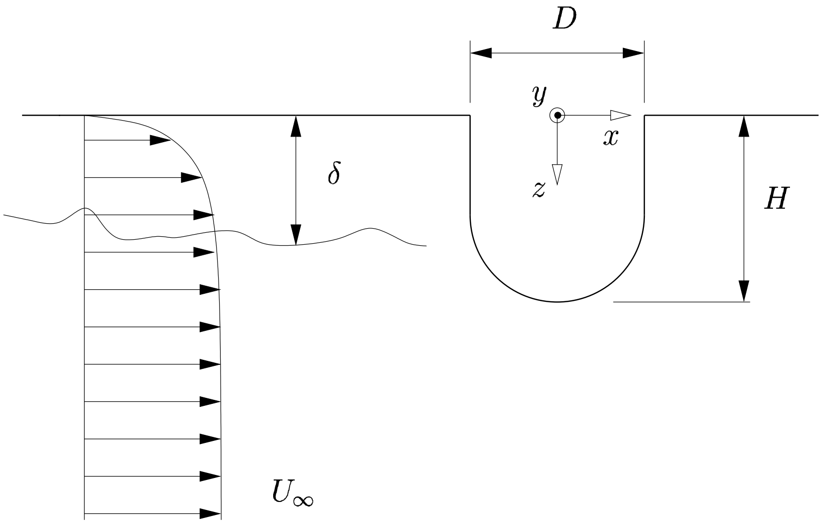

Figure 2.3: Schematic of the radome.

significant flow three-dimensionality. The end-wall effects are expected to be very different since one end-wall is mounted on a plane wall whereas the other is free. The presence of the plane wall will force the flow towards a two-dimensional state since the wall-normal velocity component is suppressed in the vicinity of the wall [11]. However, the wall-mounted radome will introduce an adverse pressure gradient which deflects the incoming two-dimensional boundary layer such as it becomes strongly three-dimensional. The three-dimensionality is mainly characterized by the continuous generation of one or more horseshoe shaped vortices that wrap around the base of the radome. These interact strongly with the near wake of the radome and the interaction is expected to increase with increased boundary layer thickness, i.e. with decreased H/δ [10].

The free end of the radome will also contribute to a significant three-dimensionalization of the flow field and continuously generate arch, or wake, vortices which shed downstream, cf. [10]. Those experimental results also suggested that these wake-vortices seem to dominate the unsteady forcing of small-aspect-ratio cylinders ($H/D < 2.5$). The importance of end-wall effects, or the wake-vortices, were further elucidated by Farvier [4] who found that the level of fluctuating pressure peaked very close to the free end, rather than in the region where the classical infinite-cylinder applies.

3 COMPUTATIONAL APPROACH

The numerical simulations are done with the commercial code Fluent 6.0, which uses the finite volume method. The accuracy of the obtained results from such simulations can be highly dependent on the spatial and temporal resolution of the simulations. The spatial resolution is given by the computational grid, while the temporal resolution is given by the time-step of the numerical solution.

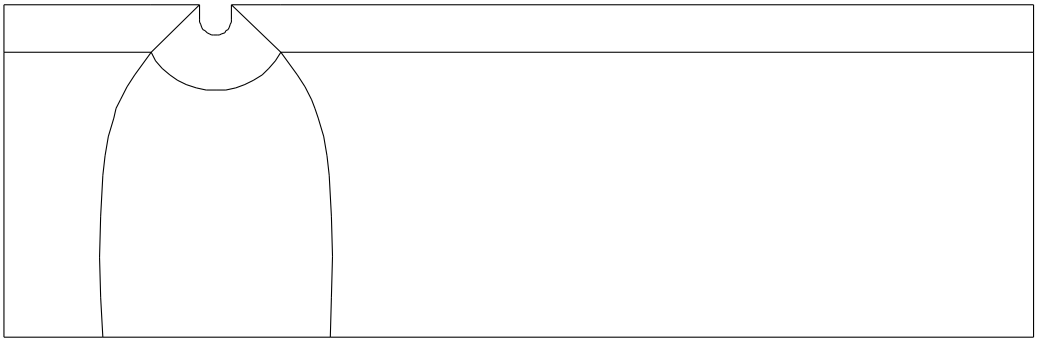

Figure 3.1: Full 21×7 *m two-dimensional geometry with subdivisions.*

The spatial grid is constructed by dividing the area around the radome into several volumes, and each of these volumes are divided into small grid cells. The goal is to make the grid inside each volume detailed enough to capture the smallest relevant features of the flow.

In the same manner that the scale of the grid cells decide how small spatial features the numerical simulation can represent, the time-step limits the accuracy of the dynamical evolution. Spatial and temporal resolution can to some extent be chosen from knowledge of the simulated physical processes, but numerical experiments are also necessary to perform simulations with the optimal balance between high physical relevance and acceptable computational time.

3.1 Two-dimensional simulations

A set of two-dimensional simulations were done as a preliminary step, to experiment with the setup for the full three-dimensional case. Because two-dimensional grids are simpler to define and change and the simulations run much faster than in three dimensions, these tests played an important role in deciding the size of the computational domain and the type of boundary conditions. The effects of compressibility were also studied in the two-dimensional simulations.

The full two-dimensional computational domain is shown in figure 3.1, which also show how the domain is divided into smaller areas to have better control of the final grid. The most important features to have in mind in the grid design are the thin boundary layer at the solid surface of the airplane body and the radome, and the separation and complex dynamics that occur in the area under and behind the radome. The grid must be detailed enough to represent these features well, with a smooth transition to areas further away where less detail is needed. A portion of the grid around the radome surface is shown in figure 3.2.

The smallest grid cells are at the solid surfaces, and the grid thickness is based on the following assumptions:

A velocity range of $90 \leq U_\infty \leq 250$ (m/s), corresponding to Mach numbers

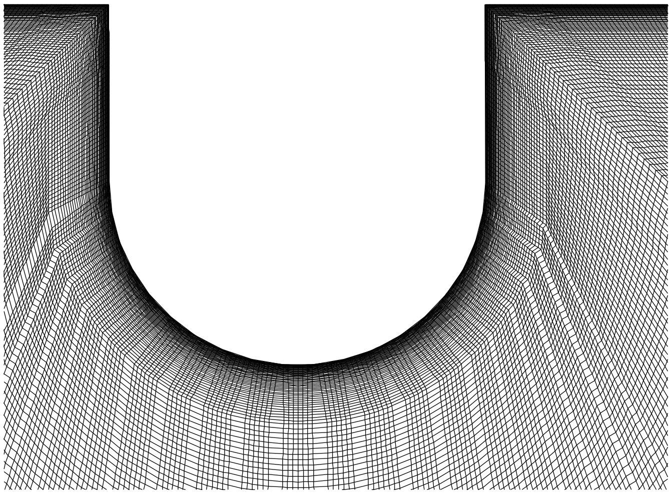

Figure 3.2: Detail of the two-dimensional grid close to the radome.

$0.26 \le M \le 0.74$, combined with a kinematic viscosity for air of $\nu = 1.5 \times 10^{-5}\,\mathrm{m}^2/\mathrm{s}$ and an approximate length scale (taken from the nose of the airplane to the radome) $L = 18$ m, give a Reynolds number ($\mathrm{Re_L} = U_\infty L/\nu$) range of $1.1 \times 10^8 \le \mathrm{Re_L} \le 3.0 \times 10^8$.

An empirical estimate for the boundary layer thickness 18 m downstream is

$$\delta = 0.37 \times 18\,\mathrm{m} \times {\mathrm{Re_L}}^{-1/4},$$

giving $0.051 \le \delta \le 0.065$ (m). The relevant lengths here are given by the dimensionless "inner length" scale

$$y^+ = y u_\tau/\nu,$$

where u_τ is the skin friction velocity given by

$$u_\tau = 0.15\,{\mathrm{Re_L}}^{-1/8}\,U_\infty.$$

For engineering turbulence simulations, the grid point closest to the wall should be in the inertial range $30 < y^+ < 300$ [5]. We choose the minimal grid cell thickness near the solid surfaces as 0.5 mm, corresponding to $58 < y^+ < 109$ for the estimated range of Reynolds numbers in this scenario.

The edge of the radome is covered by 200 cells with an average length of 8 mm, and the full two-dimensional mesh consists of approximately 143 000 cells.

Since the dynamical effects are not correctly represented in a two-dimensional model, only steady-state calculations were carried out in this case. Each of the six cases (three background velocities, incompressible and compressible) ran for about one day on four processors on SGI Origin 3800 to converge to steady state. The maximum velocity magnitude and total drag force on the radome in these simulations are given in table 3.1. Compressible effects seem to be small except for the $U_\infty = 250$ m/s case, where a shock is formed at the radome surface.

	Incompressible		Compressible	
U_∞ [m/s]	$\lvert U\rvert_{\max}$ [m/s]	F_x [N]	$\lvert U\rvert_{\max}$ [m/s]	F_x [N]
90	165	1866	170	2152
150	278	8106	287	7004
250	464	12530	408	29920

Table 3.1: Summary of two-dimensional results.

Boundary	Incompressible	Compressible
Inflow	Velocity inlet	Mass flow inlet
Outflow	Pressure outlet	Pressure outlet
Lower	Symmetry	Symmetry
Surface	Wall	Wall

Table 3.2: Boundary conditions in the two-dimensional simulations.

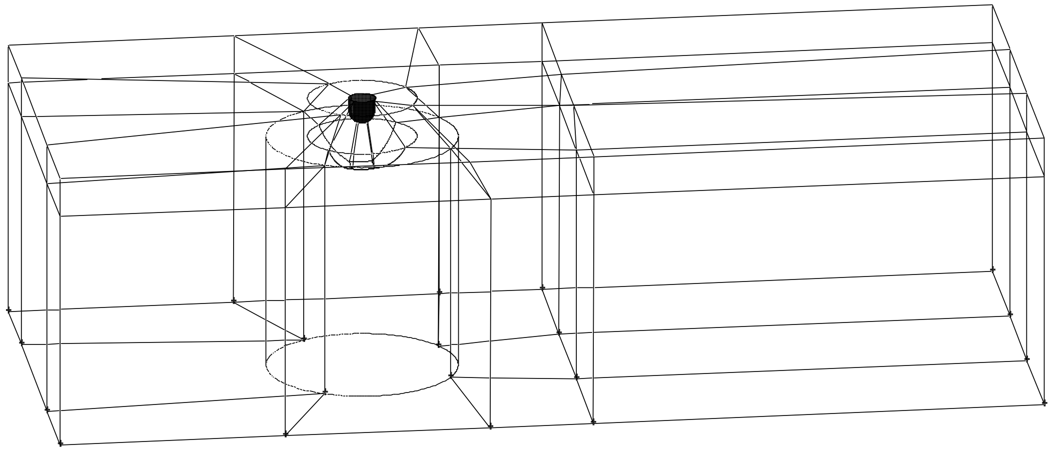

Figure 3.3: Full $24 \times 10 \times 7$ *m three-dimensional geometry with subdivisions.*

A weakness in that particular compressible simulation was that the velocity at the inflow boundary was not equal to U_∞, but varied between 200 and 225 m/s. This was presumably a consequence of having too small distance from the inflow boundary to the obstacle in front of the radome, combined with the fact that in a compressible calculation only the mass inflow can be specified, instead of setting the inflow velocity directly as in the incompressible case. Pressure far-field conditions were also tested both at the inflow and outflow boundaries, as well as specifying larger mass inflow, but neither improved the situation. To avoid this problem in future compressible simulations, the inflow boundary should be further away from the obstacle at such high speeds.

There were no problems at the other boundaries in the two-dimensional calculations, which indicates that boundary conditions were properly chosen and that the domain was sufficiently large to avoid boundary effects to interfere with the important physics around the radome. The preferred boundary conditions for the two-dimensional calculations are summarized in table 3.2.

3.2 Three-dimensional simulations

The three-dimensional grid was built up following the same principles as in two dimensions — small subvolumes around the radome mimicking its form, and larger volumes outside these to obtain a sufficiently large computational domain. The 32 subvolumes used for these simulations are shown in figure 3.3, where the radome is drawn in grey. To avoid the problems with high speed inflow mentioned in the previous section, the distance from the radome to the inflow boundary was doubled to 8 m.

As in the two-dimensional grid, the thinnest grid cells at the solid surfaces are 0.5 mm thick, and the grid resolution at the radome surface is almost as fine as in the two-dimensional grid. There are 120 cells around the radius of the cylinder, corresponding to an average cell width of 17 mm at the foot and smaller than that at the actual hemisphere.

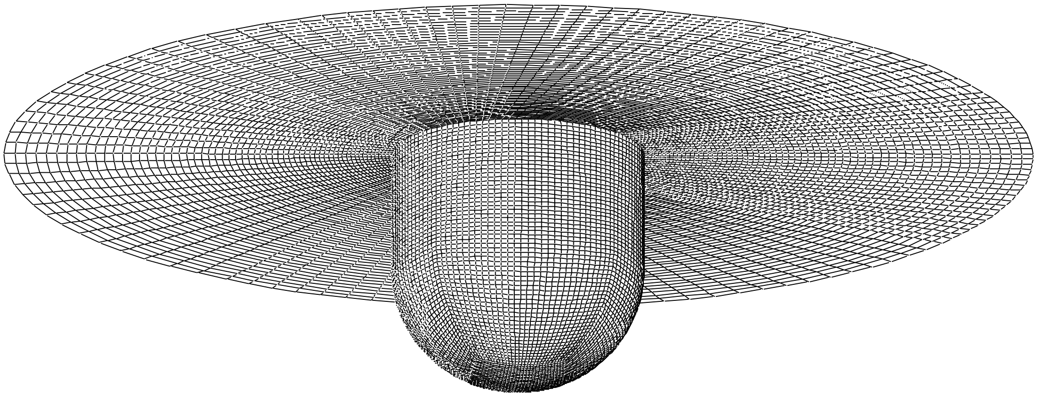

Figure 3.4: Grid at the surface of the radome and the adjacent airplane surface.

The grid is also finer at the backside of the radome than at the front, in order to resolve the important dynamical flow features in the wake, while it is fully symmetric around the $y = 0$-plane dividing the radome in the streamwise direction. The surface grid at the radome and the nearest parts of the airplane surface is shown in figure 3.4.

The main difference from the two-dimensional grid is that the three-dimensional cells grow much faster away from the surface boundary layers, to keep the total number of cells on a reasonable level. As an example, there are 50 grid points along each diagonal edge starting at the radome foot, while the corresponding edges in the two-dimensional grid had 120 grid points. Still the dominant physical effects seem to be sufficiently resolved, partly due to the fact that the three-dimensional structures are more compact than the corresponding (non-physical) effects in two-dimensional simulations.

The full three-dimensional grid consists of 1 687 500 cells, and the same boundary conditions were used as in the two-dimensional simulations, with additional symmetry boundary conditions in the transversal direction.

Three-dimensional compressible simulations were not carried out at this preliminary stage of the project, as the compressible effects observed in the two-dimensional simulations were rather small. In a more thorough investigation of these processes, compressible simulations should be done for at least the highest background velocities.

Each of the three time-dependent simulations reported in the next section ran for one to two weeks on 12 processors on SGI Origin 3800. Another important task in a further study is to search for more optimal calculations by experimenting with grids and time-steps.

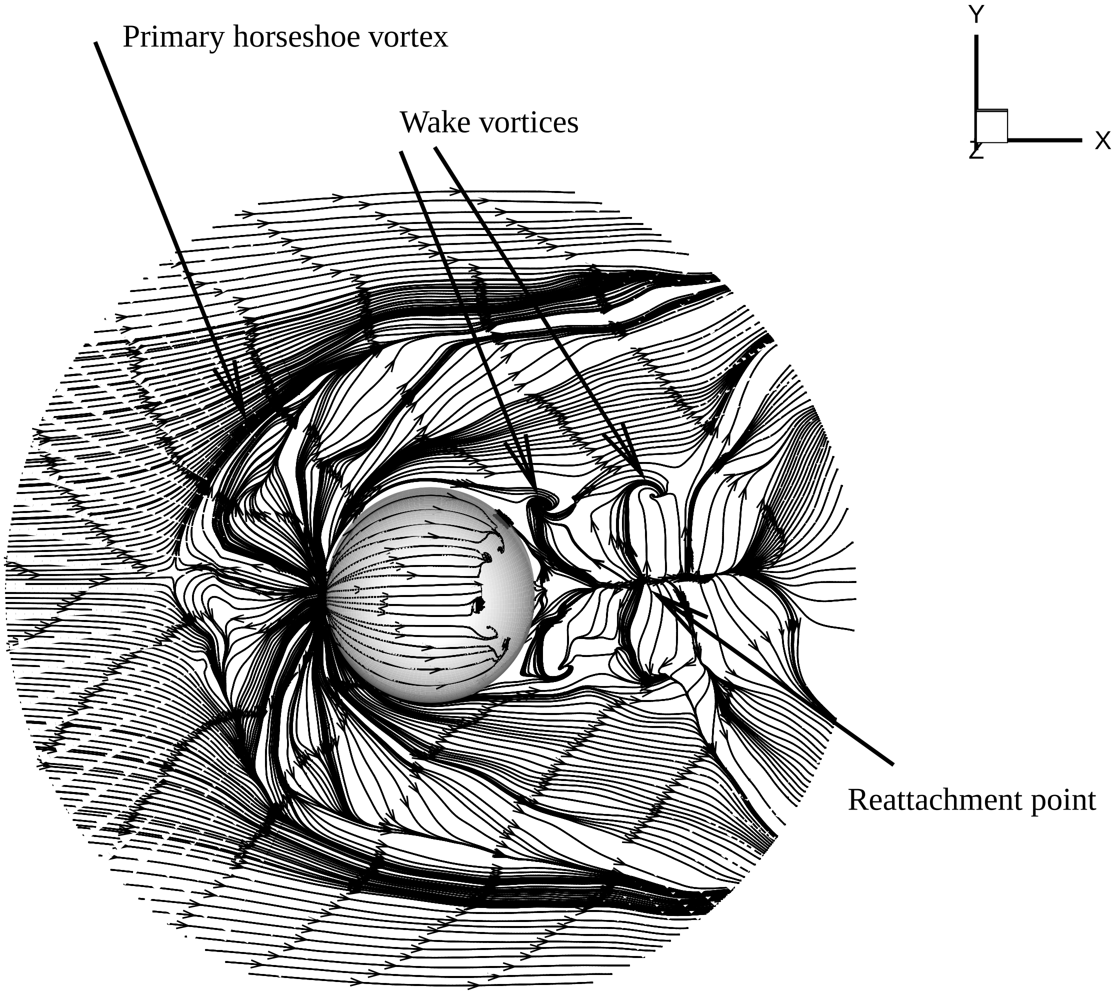
Primary horseshoe vortex
Wake vortices
Y
Z
X
Reattachment point

Figure 4.1: Instantaneous wall friction lines. Flow from left to right in the figure.

4 RESULTS

4.1 Flow field

Figure 4.1 depicts the instantaneous wall friction lines at $U_\infty = 90$ m/s. These lines display the direction of the wall shear stress along the wall, i.e. $\sim \partial U_{||}/\partial x_n$ where the subscripts $||$ and n denote the tangential and wall-normal directions at the wall, respectively These patterns reveal a very complex flow pattern, both upstream and downstream of the radome. Several vortices are formed upstream of the radome. These are folded around the base in a horseshoe shape; horseshoe vortices. Imprints of a series of wake vortices generated on the radome surface are also clearly visible in the near wake region. These flow patterns have previously been reported, which indicates that the present computations are able to reproduce some of the most dominating features observed in experimental studies, cf. e.g. [10], despite the very high Re. Another interesting feature is the separation on the spherical dome, which seems to suggest generation of concentrated vortices that would form a vortex chain. This has been noted by for instance Dallmann *et al.* [3], who consider the flow over a sphere.

Figure 4.2 shows the instantaneous streamwise wall shear stress, $\mu(\partial U/\partial x_n)|_{\text{wall}}$. The flow separation position on the radome is clearly seen, as well as the backflow associated with the horseshoe vortex upstream of the radome. It is also very encouraging that the computations seem to capture the well-known streak-like structures of the turbulent boundary layer that forms on the radome. The flow separation region downstream of the radome is relatively short, approximately D, which is a consequence of the three-dimensionality of the problem. The preliminary two-dimensional computations showed significantly larger separation regions. This invalidates any attempt to analyse this problem by two-dimensional time-dependent computations.

In an attempt to quantify the flow structures in the vicinity of the radome, isocontours of the parameter

$$Q = \frac{1}{2}\left(W_{ij}W_{ij} - S_{ij}S_{ij}\right) \tag{4.1}$$

where

$$W_{ij} \equiv \frac{1}{2}\left(\frac{\partial U_i}{\partial x_j} - \frac{\partial U_j}{\partial x_i}\right) \tag{4.2}$$

and

$$S_{ij} \equiv \frac{1}{2}\left(\frac{\partial U_i}{\partial x_j} + \frac{\partial U_j}{\partial x_i}\right) \tag{4.3}$$

denote the instantaneous vorticity and rate-of-strain, respectively, are displayed in figure 4.3. Both the horseshoe vortices (B) in front of the radome as well as the wake-vortices (A)

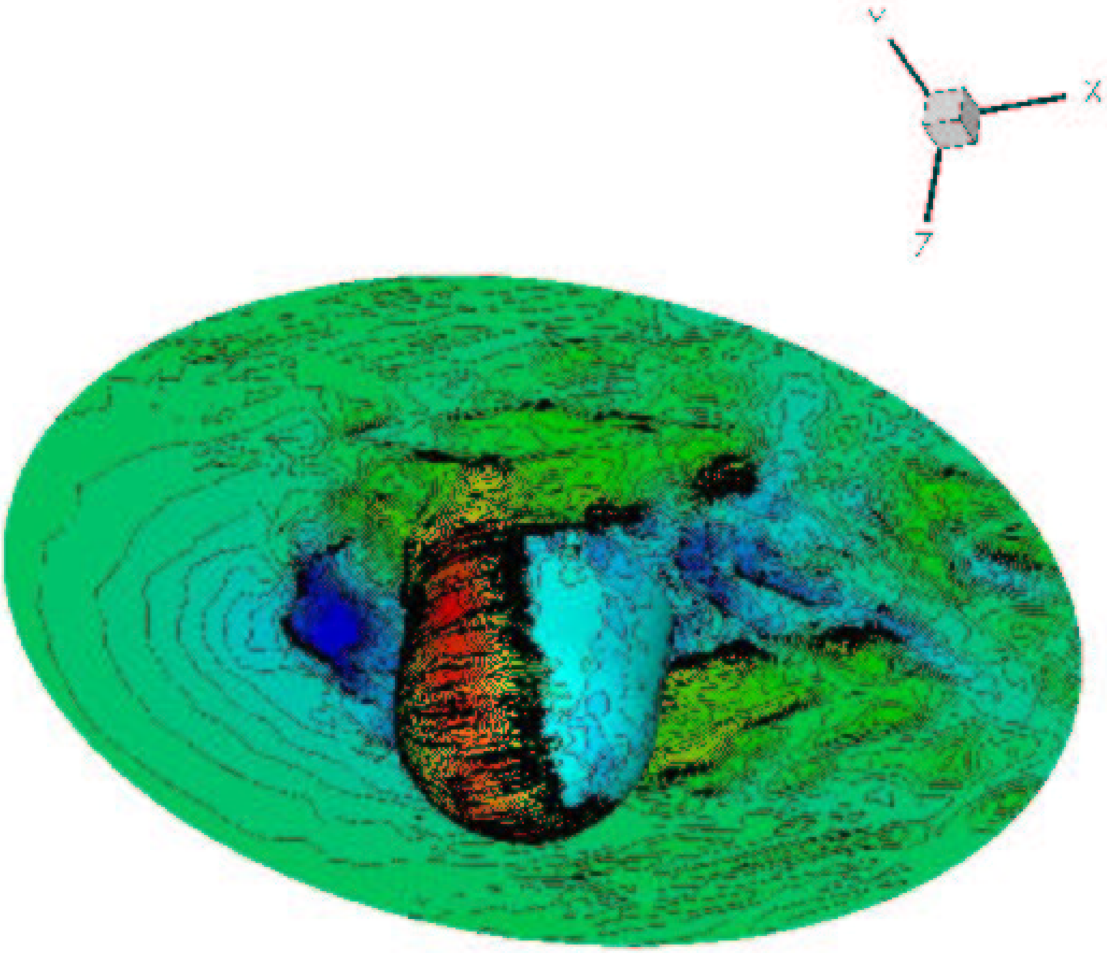

Figure 4.2: Instantaneous distribution of the wall friction in the streamwise x-direction. Blue regions indicate backflow (in the negative x-direction) whereas red regions indicate large positive shear. Flow in positive x-direction.

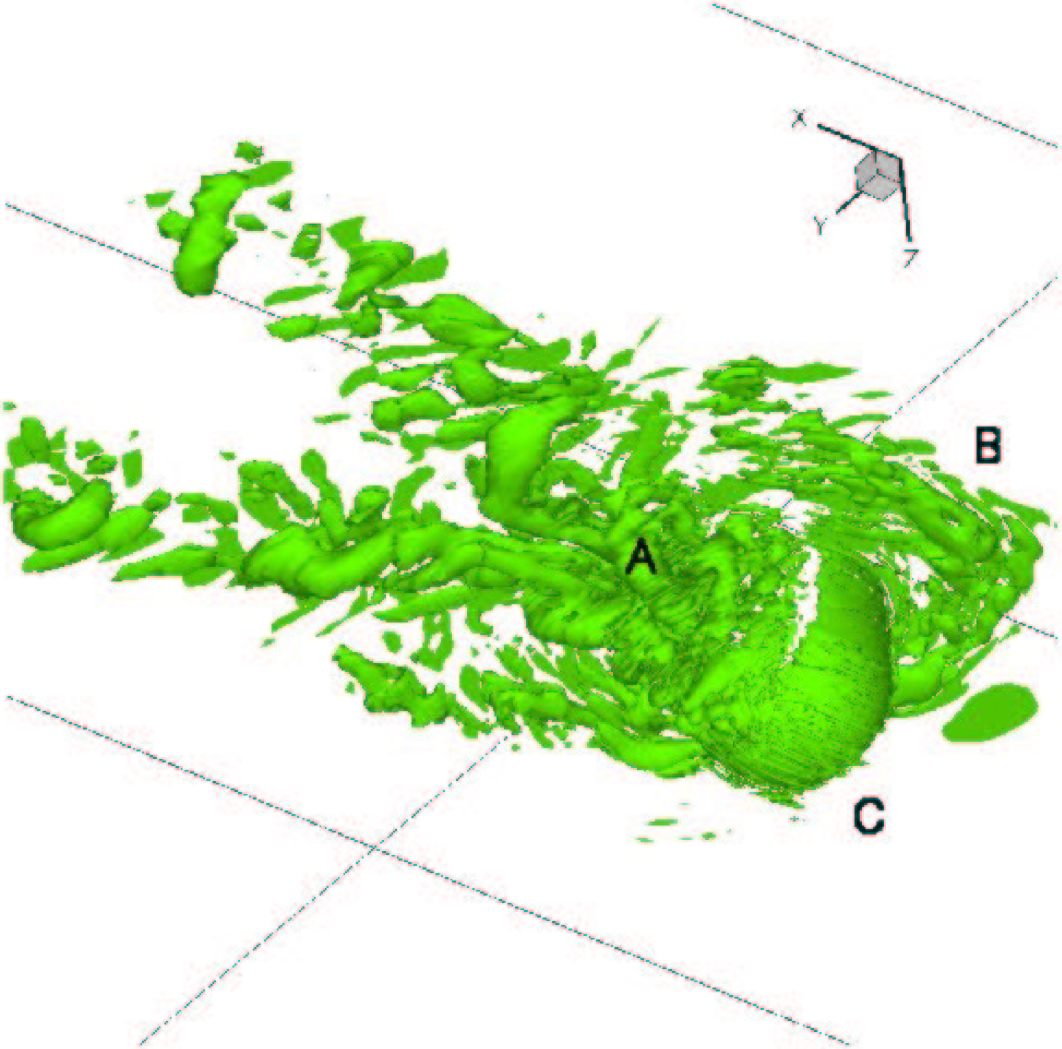

Figure 4.3: Isocontours of $Q = \frac{1}{\rho}\nabla^2 p$*. A: Wake vortices; B: Horseshoe vortices; C: Streamwise elongated vortices. Flow in positive* x*-direction.*

in the near-wake region are clearly visible. It is also very interesting to observe that the thin boundary layer on the radome consists of elongated streamwise structures (C), which is a well-known feature of turbulent boundary layers. These are fully consistent with the ’streak-like structures’ discussed above and indicated in figure 4.2. [2]

4.2 Forces

4.2.1 Available structural measurements

Previously conducted measurements [7, 8] have revealed very large amplitude vibrations. Measurements were conducted on several different locations on the aircraft, with and without the radome, and it is clear from the results that the radome caused an unsteady shedding that resulted in low frequency vibrations ($f \approx 5$ Hz). This frequency is considerably lower than what would be expected if the flow were governed by the same physical mechanisms as observed for infinite cylinders in a cross flow[3]. The challenge is thus to be able to reproduce low frequency oscillations which seem to be a consequence of the geometry of the radome rather than some universal behaviour of infinite cylinders. It is however difficult to use these experimental findings for quantitative comparisons with the simulations, so the verifications will necessarily have to be based on a qualitative assessment of the results.

4.2.2 Numerical results

Results for three different freestream velocities ($U_\infty = 90,\ 150,\ 250$ m/s) are presented in this section. The time variation of the transversal force coefficient per unit area

$$C_y \equiv \frac{F_y}{\frac{1}{2}\rho U_\infty^2}. \tag{4.4}$$

is shown in figure 4.4. Here F_y denotes the force on the radome in the y-direction. Figure 4.5 displays the corresponding power spectra

$$\Phi(f) \equiv \frac{\phi(f)}{\left(\frac{1}{2}\rho U_\infty^2 D\right)^2} \tag{4.5}$$

---

[2] Such structures can on the other hand not be observed on the plane wall. This is most likely due to an insufficient spatial resolution in the streamwise (x) and spanwise (y) directions; the computational grid is not fine enough to capture these small scale structures in this region. However, this not a major deficiency and it is not believed to invalidate any conclusions drawn from the present preliminary study.

[3] 75-130 Hz depending on the magnitude of the freestream velocity.

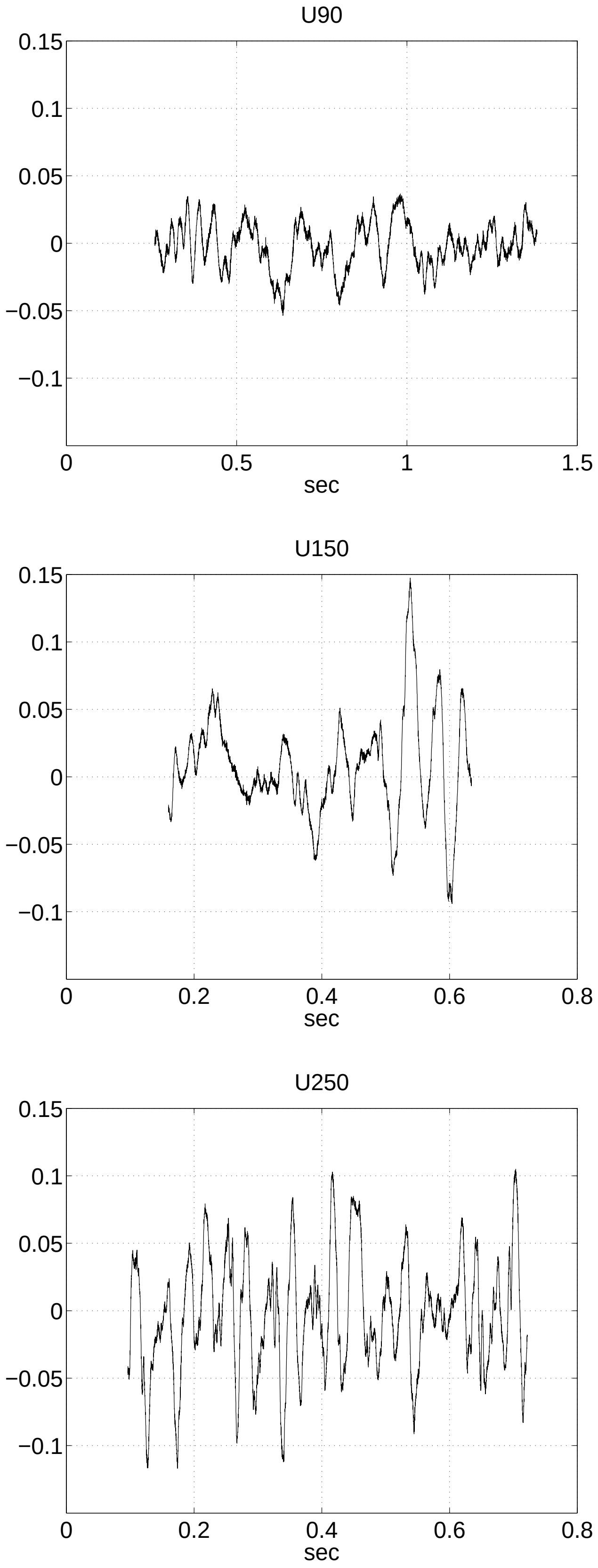

Figure 4.4: Time-evolution of the scaled transversal drag force coefficient C_y.

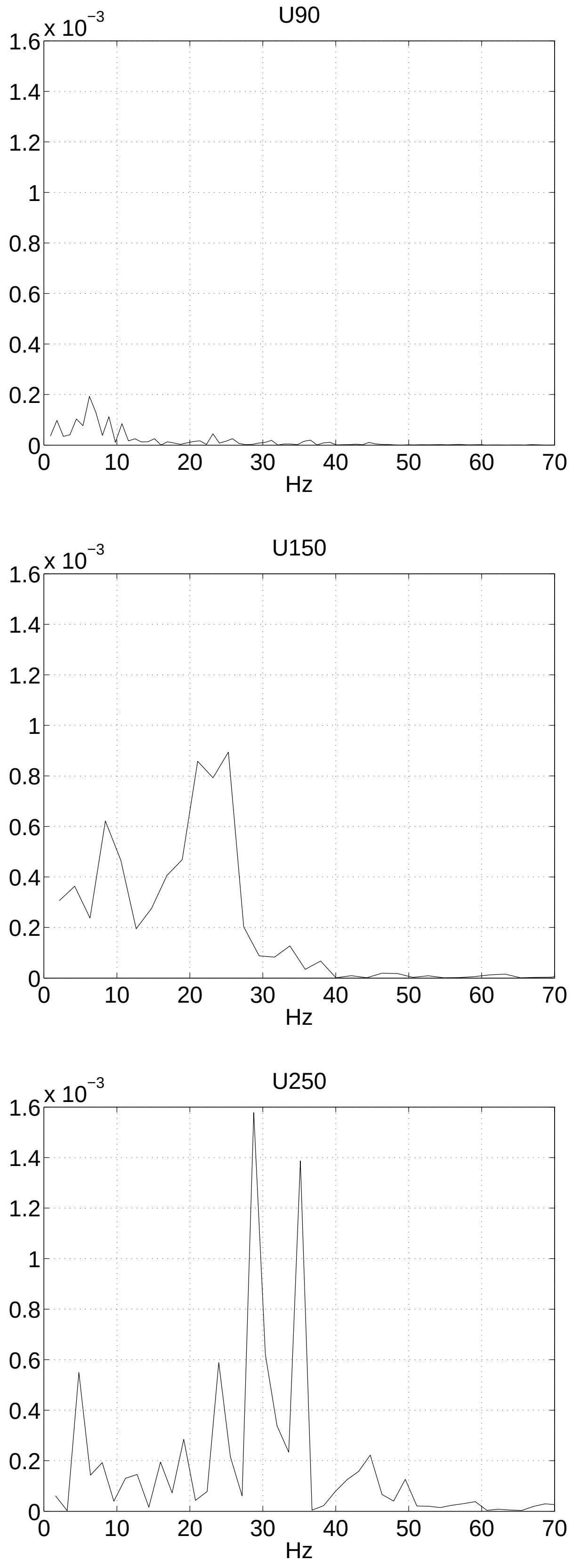

Figure 4.5: Scaled power spectra $\Phi(f)$ of the transversal drag force.

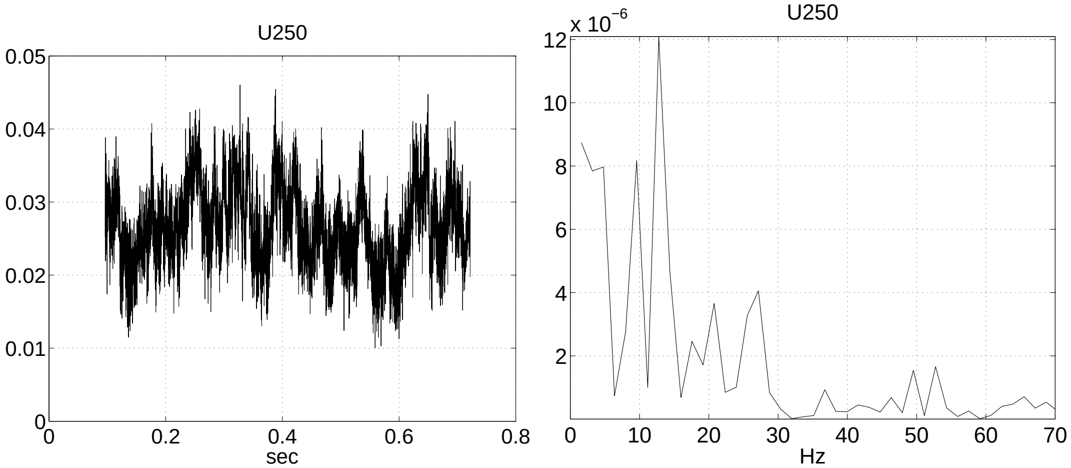

Figure 4.6: Time-evolution (left) and scaled power spectrum (right) of the scaled transversal moment Cm_y.

as a function of f, where $\phi(f)$ is the power spectrum of F_y. The amplitude and the dominating frequency of the transversal force increase with increased freestream velocity;

$$\frac{F_y^{90m/s}}{F_y^{150m/s}} \approx 0.29 \quad \text{and} \quad \frac{F_y^{150m/s}}{F_y^{250m/s}} \approx 0.25. \tag{4.6}$$

The dominating frequencies increase at $U_\infty = 150$ and $U_\infty = 250$ m/s but there exist secondary peaks at $f \approx 9$ and $f \approx 5$ Hz, respectively, that are close to the dominating frequency $f \approx 6$ Hz at $U_\infty = 90$ m/s.

During the $U_\infty = 250$ m/s computation, it was decided to also monitor the fluctuating moment about the transversal y-axis at $(x, y, z) = (0, 0, 0)$. The transversal moment coefficient per unit volume is defined as

$$Cm_y \equiv \frac{M_y}{\frac{1}{2}\rho U_\infty^2}. \tag{4.7}$$

where M_y is the moment about the y-axis, and the corresponding power spectrum

$$\Phi_m(f) \equiv \frac{\phi_m(f)}{\left(\frac{1}{2}\rho U_\infty^2 D\right)^2} \tag{4.8}$$

where $\phi_m(f)$ is the power spectrum based on M_y, are shown in figure 4.6. It is very interesting to note that the dominating frequency of the transversal moment is significantly lower than the transversal force in figure 4.5.

The present results are summarized in table 4.1. It should be noticed that the resolution of the $U_\infty = 250$ m/s computations in this preliminary study is probably marginal, and those results may therefore not be as accurate as for the two other freestream velocities.

U_∞ [m/s]	f_{F_y} [Hz]	f_{M_y} [Hz]	St	Re	$H/\delta\|_{x=-5D/2}$
90	7	—	0.05	8.5×10^6	6.5
150	25	—	0.11	1.4×10^7	8.1
250	29	13	0.08	2.4×10^7	9.7

Table 4.1: Summary of three-dimensional results.

The tendency of an increased dominating frequency with increased H/δ (or Re) is consistent with experimental results, although the magnitude of St is smaller than those reported in [10] ($\mathrm{St} \sim 0.15$) for a small aspect-ratio wall-mounted cylinder. However, this discrepancy can partly be related to the differences in geometry. In their study, Sakamoto and Arie [10] did not consider a free end with a spherical shape which is characteristic of the radome. Moreover, Dallmann *et al.* [3] argued that the dominating Strohaul frequency for a sphere is lower than for a cylindrical shape, $\mathrm{St}_{\mathrm{sphere}} \sim 0.80\,\mathrm{St}_{\mathrm{cylinder}}$, which brings our results in much closer agreement with measured structural vibrations. This observation also suggests that observed shedding might not only be attributed to the classical shedding caused by the cylinder, but instead to the spiraling vortices generated on the spherical end wall in combination with the wake-vortices. The classical Von Karman vortex street visible in figure 2.2 does consequently not seem to be the dominating physical mechanism that drives the unsteady forcing of the radome.

5 CONCLUSIONS

The objective of the present study was to establish whether or not numerical flow computations could reproduce the low frequency shedding caused by the radome observed in previous measurements [7, 8]. It has been shown that the present computations indeed capture such low frequency vibrations. The results are also in good qualitative agreement with existing literature with respect to the complexity of the flow field. It can therefore be concluded that the CFD *methodology* described in this report seems a viable tool for improved design of the radome with the objective to reduce the amplitude of the unsteady fluid forcing.

References

[1] E. Berger and R. Wille. Periodic flow phenomena. *Ann. Rev. Fluid Mech.*, 4:313–340, 1972.

[2] S.-S. Chen. *Flow-induced vibration of circular cylindrical structure.* Springer-Verlag, Berlin, 1987.

[3] U. Dallmann, H. Gebing, and H. Vollmers. Unsteady three-dimensional separated flows around a sphere - analysis of vortex chain formation. In Eckelman et al., editor, *IUTAM Symposium:Bluff-body wakes, dynamics and instabilities*, pages 22–24, 1992.

[4] D. Farvier. Turbulent flow around cylinders of finite lengh. *AIAA J.*, 19:275–281, 1981.

[5] W. K. George and L. Castillo. Zero-pressure-gradient turbulent boundary layer. *Appl. Mech. Rev.*, 50(12:1):689–729, 1997.

[6] P. Huerre and A. Monkewitz. Local and global instabilities in spatially developing flows. *Ann. Rev. Fluid Mech.*, 22:473, 1990.

[7] Ø. Lundberg. Aksellerasjonsmålinger på Orion P-3C. *FFI NOTAT*, 2000/05493, 2000.

[8] Ø. Lundberg and A. Skaugen. Nye aksellerasjonsmålinger på Orion P-3C. *FFI NOTAT*, 2002/04504, 2002.

[9] A. Roshko. Experiments on the flow past a circular cylinder at very high Reynolds number. *J. Fluid Mech.*, 10:345–356, 1961.

[10] H. Sakamoto and M. Arie. Vortex shedding from a rectangular prism and a circular cylinder placed vertically in a turbulent boundary layer. *J. Fluid Mech.*, 126:147–165, 1989.

[11] S. Szepessy and P.W. Bearman. Aspect ratio and end plate effects on vortex shedding from a circular cylinder. *J. Fluid Mech.*, 234:191–217, 1992.

DISTRIBUTION LIST

FFIBM **Dato:** 2. april 2003

RAPPORTTYPE (KRYSS AV) ☒ RAPP ☐ NOTAT ☐ RR	RAPPORT NR. 2003/01331	REFERANSE FFIBM/820/170	RAPPORTENS DATO 2. april 2003
RAPPORTENS BESKYTTELSESGRAD Unclassified		ANTALL TRYKTE UTSTEDT 29	ANTALL SIDER 27
RAPPORTENS TITTEL NUMERICAL SIMULATIONS OF FLOW-INDUCED VIBRATIONS ON ORION P-3C		FORFATTER(E) REIF Bjørn A P, WASBERG Carl Erik	
FORDELING GODKJENT AV FORSKNINGSSJEF Bjarne Haugstad		FORDELING GODKJENT AV AVDELINGSSJEF: Jan Ivar Botnan	

EKSTERN FORDELING

ANTALL	EKS NR	TIL
1		Thor Strømsnes
		Vedlikeholdsgruppen
		Andøya Flystasjon
		8480 Andenes
1		FLO/Luft/DFF
1		FLO/Luft/DF
1		v/ Oblt. Jan Hartz
1		FLO/Luft/DFP
1		v/ Maj. Truls Ørpen
1		FLO/Sjø
1		v/ Jostein Støldal

INTERN FORDELING

ANTALL	EKS NR	TIL
9		FFI-Bibl
1		FFI-ledelse
1		FFIE
1		FFISYS
1		FFIBM
1		FFIN
2		Forfattereksemplar(er)
5		Restopplag til Biblioteket
		Elektronisk fordeling:
		FFI-veven
		Øyvind Andreassen, OyA
		Thor Gjesdal, ThG
		Anders Helgeland, AHe
		Jan Olav Langseth, JOL
		Atle Ommundsen, AOm
		B. Anders P. Reif, BRe
		Elling Tveit, ETv
		Carl Erik Wasberg, CEW
		Øistein Lundberg, OiL
		Stian Løvold, StL
		John-Mikal Størdal, JMS
		Gunnar Wang, GuW

Benytt ny side om nødvendig.